nature communications

Article

https://doi.org/10.1038/s41467-026-70503-2

Multisite atomic-chlorine-passivation stabilizes perovskite interfaces for efficient H_2O_2 photosynthesis from seawater

Received: 3 September 2025

Accepted: 27 February 2026

Published online: 15 March 2026

Check for updates

Genping Meng[1,2], Shuai Wei[1,2], Ning Li[1,2], Yuhui Yin[1], Bin Dong[1], Shihao Sun[1], Guowen Hu[1], Hao Wang[1] ✉ & Baodui Wang[1] ✉

Lead halide perovskites are promising for artificial photosynthesis but suffer from aqueous instability. Here, we stabilize $CsPbI_3$ quantum dots within a hydrophobic chlorine-functionalized covalent organic framework through multisite atomic-chlorine passivation, forms dual Cl-Pb coordination and Cl-I halogen bonding at the interface. This suppresses ionic migration while creating a gas-solid-liquid triphase interface for enhanced O_2 diffusion. The resulting S-scheme heterojunction spatially separates carriers to concurrently drive two-electron oxygen reduction and water oxidation for H_2O_2 synthesis without sacrificial agents. The system achieves production rates of 20.37 mmol h^{-1} g^{-1} in seawater, with a solar-to-chemical conversion efficiency of 1.38%, and operates stably for 20 h. Importantly, natural sunlight tests yield 11.7 mmol L^{-1} H_2O_2 in 10 h. Mechanistic studies confirm synergistic interfacial charge transfer and dual-reaction pathways via both oxygen reduction and water oxidation. This work demonstrates an approach for robust perovskite-based photocatalysts toward solar-driven chemical synthesis from seawater.

Hydrogen peroxide (H_2O_2) is an indispensable chemical oxidant with burgeoning applications in water treatment, disinfection, and green synthesis[1,2]. However, the incumbent anthraquinone process for H_2O_2 production is energy-intensive, generates significant waste, and relies on centralized facilities, limiting its accessibility and sustainability. Solar-driven photosynthesis of H_2O_2 directly from water (H_2O) and oxygen (O_2) offers a compelling decentralized and sustainable alternative[3]. Seawater, constituting over 96% of Earth's hydrosphere, presents an abundant aqueous resource for this process, yet its complex ionic composition and corrosivity pose formidable challenges to photocatalyst stability and performance[4]. The development of effective, seawater-compatible photocatalytic systems is therefore essential to unlock scalable solar H_2O_2 synthesis.

Lead halide perovskites, particularly $CsPbI_3$ quantum dots (QDs), have emerged as light harvesters for artificial photosynthesis[5,6]. This is attributed to their extensive visible-light absorption, suitable band edges, and high charge-carrier mobility[7]. However, their well-known vulnerability to ionic dissolution and structural degradation in aqueous environments, especially in ion-rich seawater, limits their practical applications[8]. Although conventional encapsulation strategies using polymers or metal oxides offer some degree of barrier protection, they often impede mass transport (such as O_2 diffusion) or fail to completely suppress interfacial ion migration, which is a crucial degradation pathway[9,10]. Covalent organic frameworks (COFs) have recently gained attention as protective matrices due to their crystallinity, designable porosity, and functional versatility[11,12]. However, chlorine-functionalized COFs (COF-Cl) remain underexplored, despite the potential of atomic chlorine sites to form strong, directional bonds with perovskite surfaces through halogen interactions (Cl-I) and coordination (Cl-Pb)[13,14]. Such atomic-scale passivation could simultaneously stabilize the perovskite and enhance interfacial charge dynamics.

Herein, we introduce an interfacial engineering strategy to simultaneously passivate $CsPbI_3$ QDs against aqueous degradation and

[1]State Key Laboratory of Natural Product Chemistry, College of Chemistry and Chemical Engineering, Lanzhou University, Lanzhou, Gansu, P. R. China. [2]These authors contributed equally: Genping Meng, Shuai Wei, and Ning Li. ✉e-mail: wangh2019@lzu.edu.cn; wangbd@lzu.edu.cn

enhance their photocatalytic activity for H_2O_2 production directly from seawater (Fig. 1). We design and synthesize COFs featuring precisely positioned, multisite atomic chlorine functionalities. The COF-Cl matrix stabilizes $CsPbI_3$ QDs through dual halogen bonding (Cl-I) and coordination (Cl-Pb), effectively suppressing ionic migration while creating a hydrophobic triphase interface to enhance O_2 diffusion. Additionally, the S-scheme heterojunction forms between the $CsPbI_3$ QDs and COF-Cl, enabling efficient spatial separation of charge carriers: electrons localized on the $CsPbI_3$ QDs drive the $2e^-$ ORR, while holes retained on the COF-Cl drive the WOR. This system achieves production rates of 20.37 mmol h^{-1} g^{-1} (natural seawater) with >90% stability over 20 h in seawater and operates efficiently under natural sunlight. Through integrated experimental and theoretical analyses, we elucidate the synergistic interfacial mechanisms driving this performance. Our work provides a strategy for robust perovskite-based photosynthesis, unlocking scalable solar-driven H_2O_2 synthesis from abundant seawater.

Results

Synthesis and characterization of hydrophobic halogenated COFs and $CsPbI_3$@COF-X system

A series of hydrophobic halogenated covalent organic frameworks (COF-X: Cl, Br, I) were synthesized via Schiff-base condensation between 4,4′,4″-(1,3,5-triazine-2,4,6-triyl) trianiline and halogenated 2,5-dihaloterephthalaldehydes (Cl, Br, I) (Fig. S1). Highly crystalline materials were obtained in o-dichlorobenzene/n-BuOH/6 M HAc (5:5:1, v/v) at 120 °C for 72 h. Structural analysis confirmed successful synthesis and high crystallinity. Powder X-ray diffraction (PXRD) patterns (Fig. S2) showed prominent (100) peaks at 2.79°, 2.75°, and 2.70° for COF-Cl, COF-Br, and COF-I, respectively, matching simulated AA stacking models (Figs. S3–S5, Table S1). Solid-state ^{13}CNMR revealed the characteristic imine peak (~160 ppm, Figs. S6–S9). Fourier transform infrared (FTIR) spectra (Fig. S10) confirmed Schiff-base formation by the disappearance of precursor -NH_2 (3213, 3327 cm^{-1}) and aldehyde (1688 cm^{-1}) stretches and the appearance of -C = N stretches (1633 cm^{-1}) for all three COF-X[15]. COF-X exhibits mesoporosity with type IV isotherms (Fig. S11). Brunauer-Emmett-Teller (BET) surface areas decreased with increasing halogen size: 2289.7 m^2 g^{-1} (COF-Cl), 1757.0 m^2 g^{-1} (COF-Br), 1150.9 m^2 g^{-1} (COF-I), correlating with pore diameters of 3.53 nm, 3.09 nm, and 2.63 nm, respectively (Table S2). Scanning electron microscope (SEM) and transmission electron microscope (TEM) images (Figs. S12, S13) revealed uniform fibrous morphologies and layered structures, with visible pores in COF-X HRTEM (Fig. S13b). X-ray photoelectron spectra (XPS) confirmed elemental composition (Figs. S14–S16). Water contact angles of 143.0°, 145.5°, and 147.5° (Fig. S17) demonstrate increasing hydrophobicity with halogen size. The thermal stability was confirmed by TGA, showing negligible weight loss at 150 °C (Fig. S18). These results confirm the successful synthesis of crystalline, mesoporous, hydrophobic halogenated COFs.

A sequential deposition route was employed to synthesize $CsPbI_3$@COF-X composites (Fig. S19). Concretely, COF-X matrices were immersed in a PbI_2 precursor solution at 70 °C. Residual PbI_2 was removed via centrifugation using DMF/ethanol. The resulting PbI_2@COF-X intermediates were then dispersed in a CsI-containing DMF solution under ultrasonication. Finally, the reaction mixture was

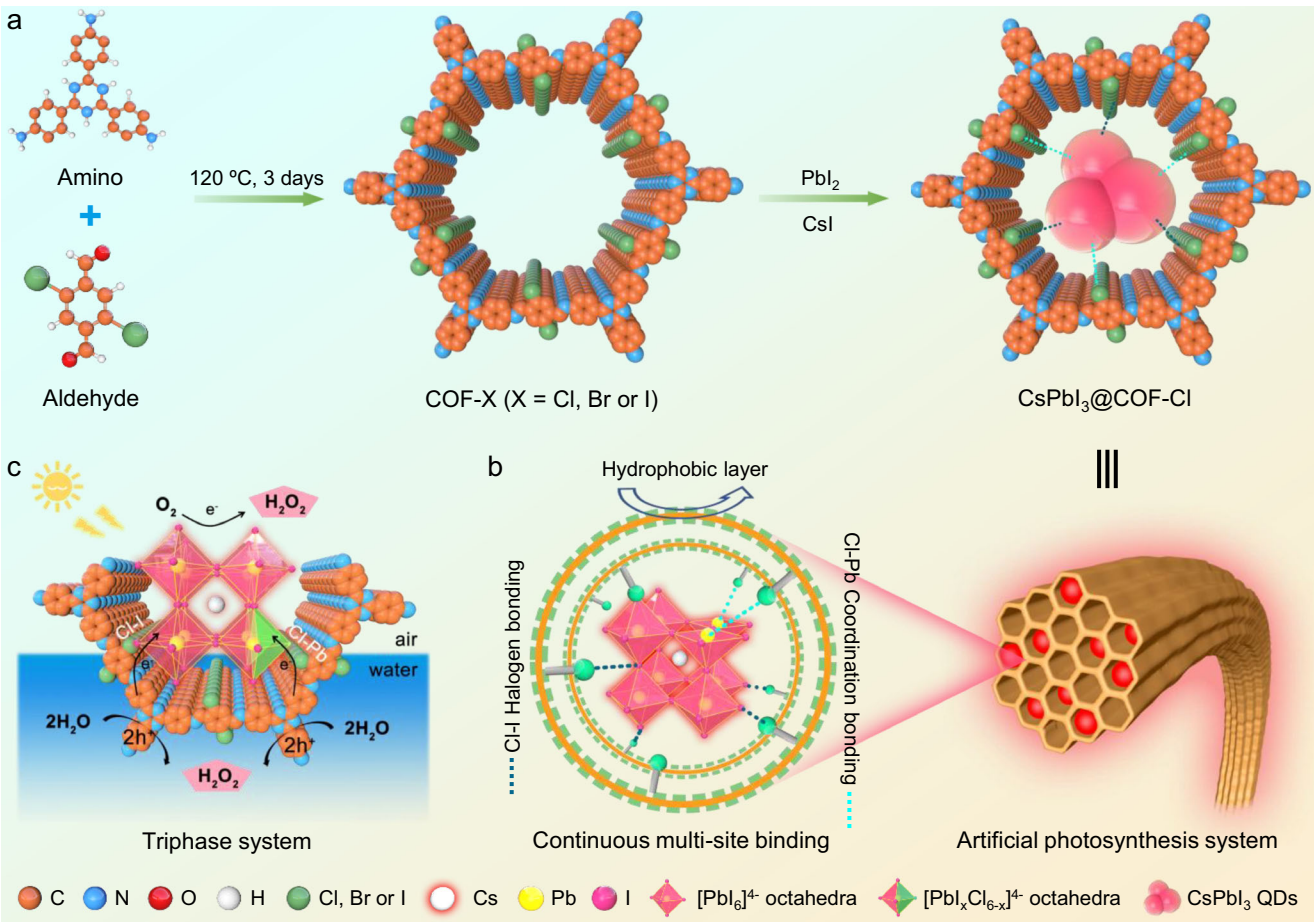

Fig. 1 | The schematic diagram of the synthesis of the triphase interface artificial photosynthetic system $CsPbI_3$@COF-X (X = Cl, Br, I). a Synthesis route of the $CsPbI_3$@COF-X system. **b** Continuous in situ passivation mechanism of COF-Cl matrix on $CsPbI_3$ QDs. **c** Photochemical synthesis of H_2O_2 at the triphase interface in the $CsPbI_3$@COF-Cl system.

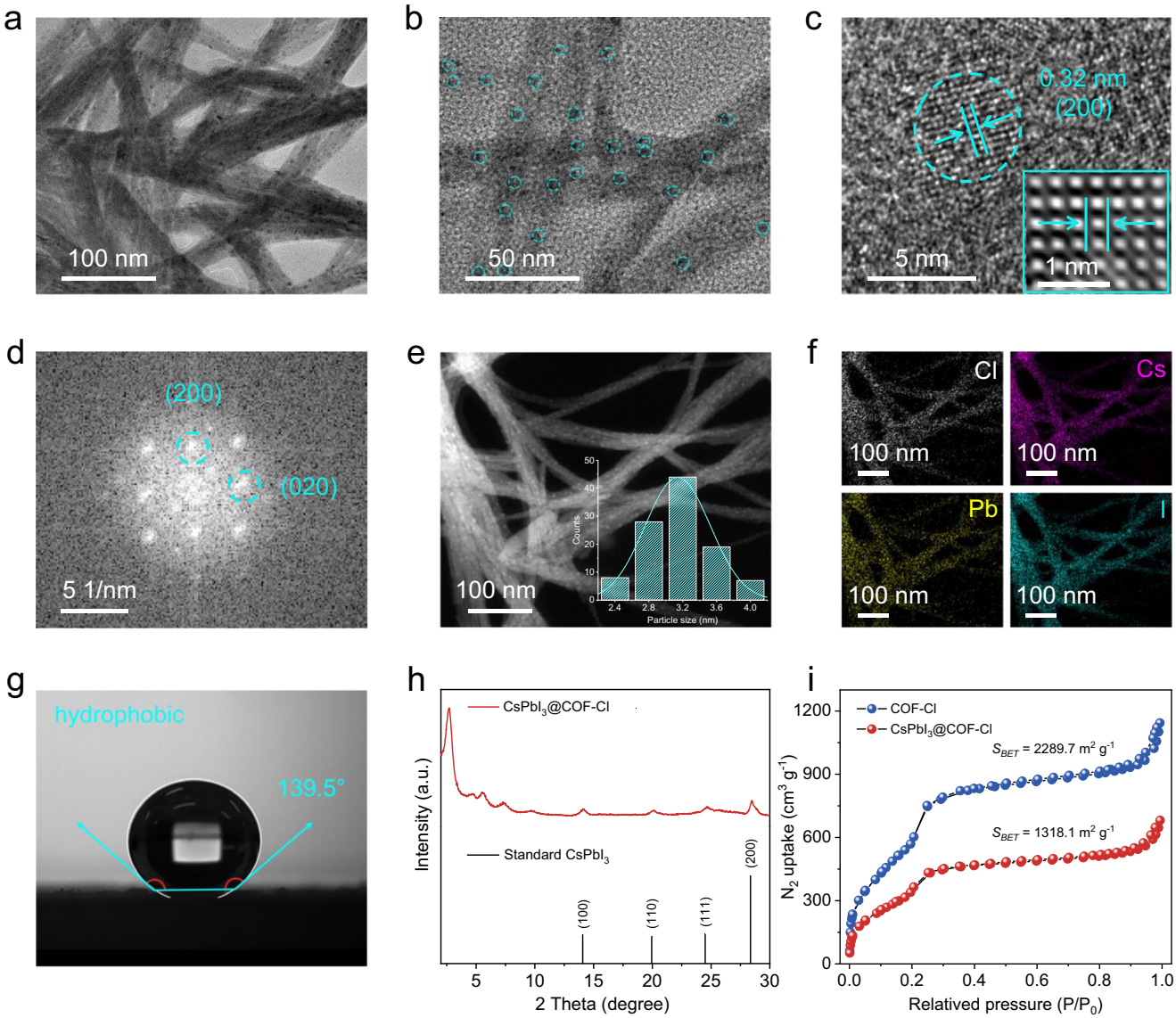

Fig. 2 | Structural and physicochemical characterizations of the $CsPbI_3$@COF-Cl system. a, **b** TEM images showing $CsPbI_3$ QDs (black dots) confined within the COF-Cl matrix. **c** HRTEM image with lattice spacing of confined $CsPbI_3$ QD in $CsPbI_3$@COF-Cl system. Inset: Magnified view of the $CsPbI_3$ QD showing atomic arrangement. **d** Fast-Fourier transform pattern corresponding to the $CsPbI_3$ QDs, confirming their high crystallinity. **e** HAADF-STEM image of the $CsPbI_3$@COF-Cl system. Inset: Size distribution histogram of the confined $CsPbI_3$ QDs. **f** EDX elemental mapping showing the spatial distribution of Cl, Cs, Pb, and I within the same region. **g** Contact angle measurements on a pressed tablet of the $CsPbI_3$@COF-Cl system. **h** PXRD pattern of the $CsPbI_3$@COF-Cl system. **i** N_2 sorption isotherms at 77 K and corresponding Brunauer-Emmett-Teller (BET) surface area plots for pristine COF-Cl and the $CsPbI_3$@COF-Cl system. Source data are provided as a Source Data file.

precipitated into toluene at room temperature (~25 °C) to obtain a series of $CsPbI_3$@COF-X systems, where $CsPbI_3$ QDs in situ nucleated and crystallized inside the COF-X matrix (for details, see the Methods section). Taking the $CsPbI_3$@COF-Cl system as an example, we demonstrate how the framework and topology of the COF-Cl matrix direct the confined growth of $CsPbI_3$ QDs. Structural characterization confirmed the successful synthesis of $CsPbI_3$@COF-Cl. SEM imaging (Fig. S20) revealed that the external surfaces of the COF-Cl matrix remained clean without observable aggregates of $CsPbI_3$ QDs, indicating their successful embedding within the matrix. TEM analysis (Fig. 2a, b, S21) further shows $CsPbI_3$ QDs uniformly dispersed within the mesoporous channels of the COF-Cl matrix. Isolated $CsPbI_3$ QDs with an average diameter of 3.2 nm are clearly resolved (Fig. 2a), which closely matches the theoretically predicted mesopore diameter range of 3.13–4.01 nm (Fig. S3b, Table S1). This close size correlation is highly suggestive of size-constrained growth within the porous network. High-resolution TEM (HRTEM, Fig. 2c) displays distinct lattice fringes (0.32 nm spacing), matching the (200) planes of α-$CsPbI_3$ (space group *Pm-3m*). The crystalline structure is further confirmed by fast-Fourier transform (FFT) patterns (Fig. 2d). STEM-HAADF imaging (Fig. 2e) corroborates the uniform dispersion of 3.2 nm $CsPbI_3$ QDs within the COF-Cl framework. Elemental mapping (EDX, Fig. 2f) confirms homogeneous distribution of Cl, Cs, Pb, and I throughout the composite. Hydrophobicity, critical for aqueous applications, was evaluated via contact angle measurements (Fig. 2g). The $CsPbI_3$@COF-Cl system exhibits apparent hydrophobicity (contact angle of 139.5°), which originates from the hydrophobic COF-Cl matrix. This property allows the lightweight composite to float and spread uniformly on the water surface (Fig. S22), establishing a distinct gas-solid-liquid (air-catalyst-water) triphase interface. To further verify the formation and function of this triphase architecture, we performed comparative electrochemical impedance spectroscopy (EIS) under two configurations:

https://doi.org/10.1038/s41467-026-70503-2

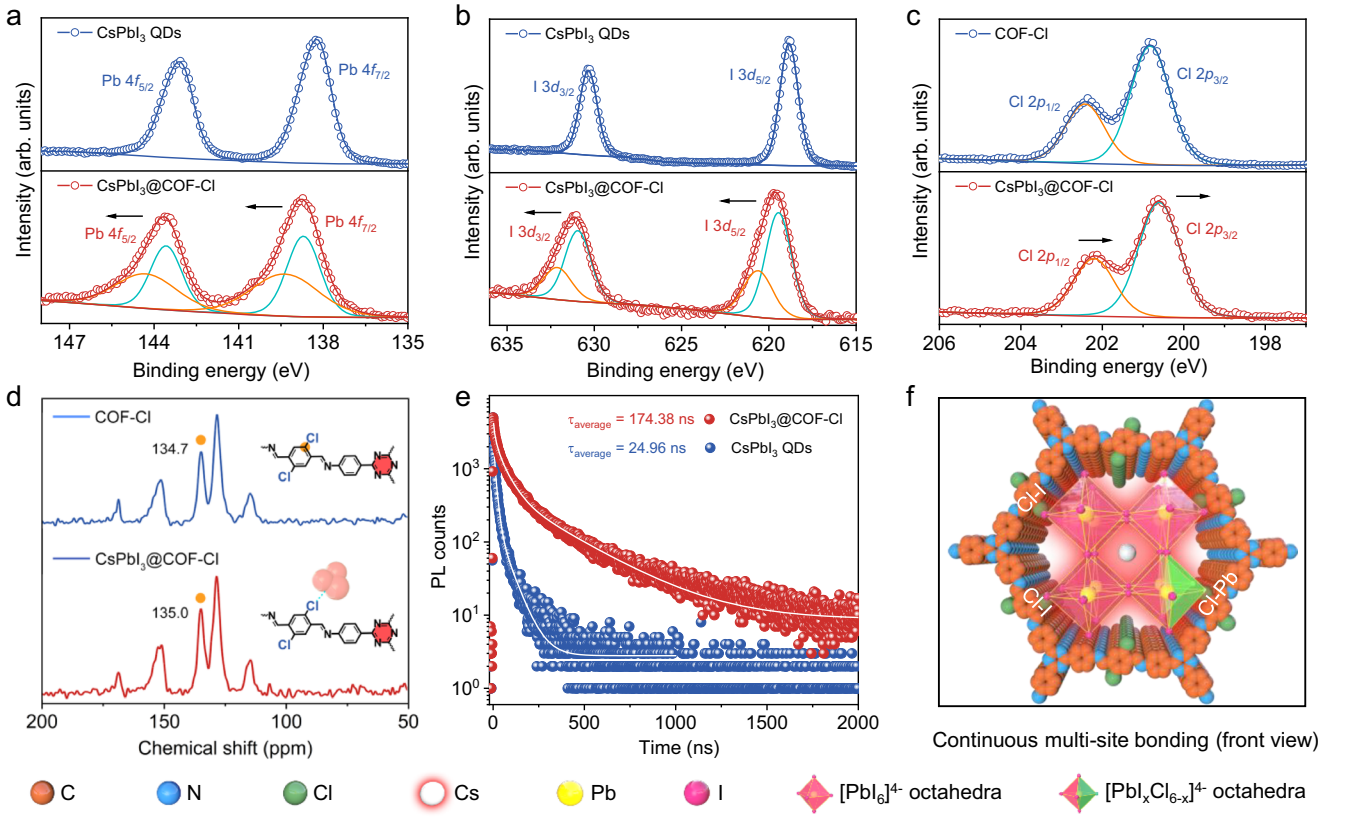

Fig. 3 | Evaluation of interaction mechanisms between the COF-Cl matrix and $CsPbI_3$ QDs in the $CsPbI_3$@COF-Cl system. a High-resolution Pb 4*f* XPS spectra of $CsPbI_3$ QDs and the $CsPbI_3$@COF-Cl system. **b** High-resolution I 3*d* XPS spectra of $CsPbI_3$ QDs and the $CsPbI_3$@COF-Cl system. **c** High-resolution Cl 2*p* XPS spectra of the COF-Cl matrix and the $CsPbI_3$@COF-Cl system. **d** Solid-state ^{13}C NMR spectra of the COF-Cl matrix and the $CsPbI_3$@COF-Cl system. **e** TRFDS of $CsPbI_3$ QDs and the $CsPbI_3$@COF-Cl system. White curves represent fitting curves. **f** Schematic illustration of the COF-Cl matrix showing continuous multisite bonding on the surface of $CsPbI_3$ QDs (front view). Source data are provided as a Source Data file.

with the catalyst fully immersed (diphasic liquid-solid interface) and with it floating at the air-water interface (triphase interface). A clear reduction of ~70% in charge-transfer resistance was observed under the floating configuration (Fig. S23), providing direct electrochemical evidence that the triphase interface enhances mass transport (particularly O_2 diffusion) and interfacial charge-transfer kinetics (Fig. S24). PXRD analysis (Fig. 2h) verifies crystallinity, with peaks at 14.1°, 19.9°, 24.5°, and 28.4° corresponding to the (100), (110), (111), and (200) planes of α-$CsPbI_3$ material (PDF No. 01-080-4039)[16]. N_2 adsorption-desorption isotherms (Fig. 2i) and the corresponding pore size distribution curves (Fig. S25) provide compelling evidence for the confinement of $CsPbI_3$ QDs within the COF-Cl mesochannels. The pore size distribution of pristine COF-Cl shows a predominant pore diameter centered at ~3.10 nm (range: 2–4 nm). For the $CsPbI_3$@COF-Cl composite, a clear reduction in the pore volume signal within this characteristic range is observed. Synchronously, the BET specific surface area plummets from 2289.7 $m^2 g^{-1}$ (COF-Cl) to 1318.1 $m^2 g^{-1}$, and the pore volume decreases from 1.77 $cm^3 g^{-1}$ to 1.05 $cm^3 g^{-1}$ (Table S2). This substantial reduction in both accessible surface area and internal pore volume is a direct signature of pore filling or occupancy by the in situ grown $CsPbI_3$ QDs. Combined with the close match between $CsPbI_3$ QD size and host pore dimensions, this data confirms that the $CsPbI_3$ QD growth is effectively confined within the accessible mesoporous channels of the crystalline COF-Cl framework, rather than merely occurring on external surfaces or between loosely packed structures. Inductively coupled plasma optical emission spectrometry (ICP-OES) analysis after complete digestion of the composite confirmed a $CsPbI_3$ QD loading of 21.2 wt% within the COF-Cl matrix. Collectively, these results confirm the successful construction of the $CsPbI_3$@COF-Cl.

To investigate the interfacial interactions between the COF-Cl matrix and $CsPbI_3$ quantum dots (QDs), we employed X-ray photoelectron spectroscopy (XPS), solid-state ^{13}C nuclear magnetic resonance (NMR) spectroscopy, and time-resolved fluorescence decay spectroscopy (TRFDS) to probe the electronic and chemical environments of the constituent elements. XPS survey spectra confirmed the presence of C, N, Cl, Cs, Pb, and I in the $CsPbI_3$@COF-Cl composite (Fig. S26), verifying its successful synthesis. In the deconvoluted Pb 4*f* spectrum of $CsPbI_3$@COF-Cl (Fig.3a, Table S3), the higher-binding-energy doublet (orange curves) is assigned to surface Pb^{2+} ions engaged in direct Cl-Pb coordination with the COF-Cl matrix, while the lower-binding-energy doublet (green curves) corresponds to bulk Pb^{2+} ions within the $CsPbI_3$ QD core, which are shielded from direct interfacial contact. Similarly, the I 3*d* spectra (Fig.3b) show a higher-binding-energy doublet (orange curves) arising from surface I^- ions directly involved in Cl-I halogen bonding with COF-Cl, whereas the lower-binding-energy doublet (green curves) originates from bulk I^- ions in the $CsPbI_3$ QD interior. Conversely, the Cl 2*p* peaks shift toward lower binding energy in the composite (Fig.3c), further evidencing a clear chemical interaction.

A detailed comparative XPS analysis of the $CsPbI_3$@COF-Br and $CsPbI_3$@COF-I composites reveals fundamentally different interfacial chemistries that explain their inferior performance. In the $CsPbI_3$@COF-Br system, the Pb 4*f* spectrum shows a large positive binding energy shift (Δ = +2.15 eV, Fig. S27a, Table S4), indicating electron transfer due to Br-Pb coordination. However, the Br 3*d* binding energy shows only a minimal negative shift (Δ = −0.05 eV, Fig. S27c, Table S4), suggesting a lack of effective electron compensation via halogen bonding. This unbalanced interaction likely leads to

interfacial charge accumulation and reduced stability. Most critically, the $CsPbI_3$@COF-I system reveals interfacial incompatibility and degradation. The deconvolution of its I 3*d* spectrum requires three distinct doublets (Fig. S28, Table S5). Besides peaks for bulk $CsPbI_3$ I^- and interfacial I^- interacting with COF-I, a third component at a very high binding energy (Δ = +3.75 eV) unequivocally confirms the oxidation of interfacial I^- to species such as I_2 or IO_x. This demonstrates that COF-I not only fails to passivate the $CsPbI_3$ surface but also actively induces detrimental interfacial reactions. In stark contrast, the $CsPbI_3$@COF-Cl system exhibits a synergistic, bidirectional electron redistribution profile with a moderate positive shift for Pb (Δ = +1.17 eV, Fig. 3a) and a concurrent negative shift for Cl (Δ = −0.22 eV, Fig. 3c), which definitively proves the coexistence of stable Cl-Pb coordination and Cl-I halogen bonding. To further verify the specific chemical interaction between COF-Cl and the $CsPbI_3$ QDs, we extended XPS analysis to the PbI_2@COF-Cl composite. The spectra reveal a distinct positive shift in the binding energy for both Pb and I in the composite compared to pristine PbI_2 (Figs. S29, S30, Table S6). This positive shift is highly similar to that observed in the $CsPbI_3$@COF-Cl system. Most definitively, the physically mixed sample (PM-$CsPbI_3$/COF-Cl) shows no discernible peak splitting or significant binding-energy shifts relative to the pristine components (Fig. S31, Table S7), confirming that the spectral changes in the in-situ composites are not artifacts of physical proximity but arise from chemically bonded interfaces formed during synthesis. The established trend in Pb-X bond strength (Pb-Cl > Pb-Br > Pb-I) provides a fundamental chemical rationale for the favorable stability afforded by the Cl-based interface[17–19].

To further investigate the chemical environment changes, solid-state ^{13}C NMR spectroscopy was performed. The spectrum (Figs. 3d, S32) revealed a downfield shift of 0.3 ppm for the carbon atoms directly bonded to chlorine in $CsPbI_3$@COF-Cl relative to pristine COF-Cl. This shift provides evidence for the formation of halogen-halogen (Cl-I) bonds and coordination interactions (Cl-Pb) at the interface. To directly assess the impact of these interactions on defect passivation, TRFDS measurements were conducted (Fig. 3e, Table S8). Fluorescence decay curves were fitted to a tri-exponential model, where fast decay correlates with surface/crystal defects and slow decay with carrier transport. Pristine $CsPbI_3$ QDs exhibited rapid decay (τ_1 = 3.13 ns, τ_2 = 13.68 ns, τ_3 = 62.22 ns; τ_{av} = 24.96 ns), attributed to non-radiative recombination from Pb-I antisite defects and vacancies[20]. In contrast, $CsPbI_3$@COF-Cl showed slower decay (τ_1 = 9.60 ns, τ_2 = 57.52 ns, τ_3 = 289.41 ns; τ_{av} = 174.38 ns), demonstrating that COF-Cl passivates defects via halogen-halogen bonds and coordination interactions, thereby suppressing non-radiative pathways[20]. Moreover, TRPL decay dynamics provide direct evidence that the performance of $CsPbI_3$@COF-Cl stems from its effective interfacial passivation. The measured lifetimes for the composites follow a definitive trend: $CsPbI_3$@COF-Cl exhibits the longest decay components and an average lifetime greater than those of $CsPbI_3$@COF-Br (τ_{av} = 106.78 ns) and $CsPbI_3$@COF-I (τ_{av} = 24.68 ns) (Figs. S33, S34, Table S8).

To elucidate the multi-site bonding mechanism depicted schematically in Fig. 3f, we investigated in detail the adsorption of the halogen-rich porous COF-Cl matrix onto $CsPbI_3$ QD surfaces, together with the corresponding binding and formation energies. Preliminary computational modeling (Figs. S35, S36), based on idealized periodic surface models, suggests that the periodic architecture of COF-Cl enables continuous multi-site bonding with the perovskite surface. Specifically, on a Pb-rich surface, adjacent-Cl groups can form a sequential chain of coordination bonds (Cl-Pb) with neighboring under-coordinated Pb^{2+} sites. Similarly, on an I-rich surface, they form a continuous network of halogen bonds (Cl-I) with consecutive I^- sites. Within the constraints of our simplified DFT models, this continuous multi-site passivation, saturating contiguous chains of surface defects rather than capping isolated sites sparsely, creates a robust interfacial network. To probe the advantage of this continuous multi-site mode over isolated passivation, we performed controlled Density Functional Theory (DFT) calculations. We compared the ideal continuous model against an artificially created discontinuous model, where specific Cl groups were removed from the framework to prevent contiguous bonding (Figs. S37, S38). The formation energy for establishing the continuous Cl-Pb network was profoundly more favorable (−2.76 eV) than for the discontinuous case (−1.28 eV). A similar trend was observed for Cl-I bonding (−2.56 eV vs. −0.80 eV) (Fig. S39a). The average binding energy per site was also stronger in the continuous configuration (Fig. S39b). This computational evidence suggests that, under the ideal conditions of our models, passivating a sequence of neighboring defects is energetically synergistic; interaction at one site favorably pre-configures the environment for the next, leading to collective stabilization and a more robust interface. Furthermore, limited molecular dynamics (MD) simulations under simplified conditions indicate that structural stability is conferred by this continuous network. In these simulations, the root mean square deviation (RMSD) of atomic positions for systems with continuous Cl-Pb/I passivation stabilizes quickly and remains consistently lower than for systems with discontinuous passivation throughout the simulation (Fig. S40), hinting at reduced interfacial atomic displacement and fluctuation.

Characterizations of the electronic properties and the band edge positions

Based on the ultraviolet-visible diffuse reflection spectra (UV-vis DRS), the COF-X matrix exhibits adsorption peaks (Soret band) around 350–500 nm (Fig. 4a), attributed to its periodic molecular framework and long-range ordered π-stacking structure. In contrast, $CsPbI_3$ QDs show a broad absorption band extending to 700 nm, indicative of a narrow bandgap. Upon encapsulation of $CsPbI_3$ QDs by COF-X to form the $CsPbI_3$@COF-X system, the absorption edge of the $CsPbI_3$@COF-X system undergoes a significant redshift beyond 700 nm, enabling more efficient solar energy utilization. This redshift clearly demonstrates the synergistic effect between COF-X and $CsPbI_3$ QDs. Tauc plot analysis (Fig. S41) determined the bandgap energies (E_g) of COF-Cl, COF-Br, COF-I, and $CsPbI_3$ QDs to be 2.50 eV, 2.58 eV, 2.49 eV, and 1.77 eV, respectively, confirming their semiconductor nature. For efficient photocatalytic reactions, the electronic band structure must align with the relevant redox potentials. Valence band XPS spectra (VB-XPS, Fig. S42) measured the valence band maximum (E_{VB}) positions relative to the vacuum level ($E_{VB,\ XPS}$). After conversion to the standard hydrogen electrode (NHE) scale, the $E_{VB,\ NHE}$ values are: COF-Cl (2.52 eV), COF-Br (2.39 eV), COF-I (2.27 eV), and $CsPbI_3$ QDs (0.94 eV). The resulting band diagrams are plotted in Fig. 4b. Importantly, this staggered band alignment satisfies the prerequisite for forming an S-scheme heterojunction. The results indicate that $CsPbI_3$ QDs possess strong reducing capabilities, while the COF-X matrices exhibit high oxidizing capabilities, with COF-Cl showing the strongest oxidizing potential (EVB = +2.52 V vs. NHE) compared to COF-Br (+2.39 V) and COF-I (+2.27 V). This deeper valence band position of COF-Cl signifies a stronger oxidation capability and promotes the formation of a larger built-in electric field at the heterojunction interface, providing a greater driving force for charge separation. This favorable energy level alignment within the $CsPbI_3$@COF-Cl composite not only maximizes the redox capabilities of the individual components but also facilitates the construction of an efficient S-scheme heterojunction (Fig. 4c). The $CsPbI_3$@COF-Cl system enhances charge transfer and carrier separation. Photoluminescence (PL) spectroscopy and TRFDS show substantially quenched PL intensity and prolonged fluorescence lifetime in $CsPbI_3$@COF-Cl compared to pure $CsPbI_3$ QDs (Figs. S43, 3e), indicating suppressed electron-hole recombination due to spatial charge separation. These properties directly improve photochemical conversion activity. Photocurrent response tests (Fig. S44) show faster

https://doi.org/10.1038/s41467-026-70503-2

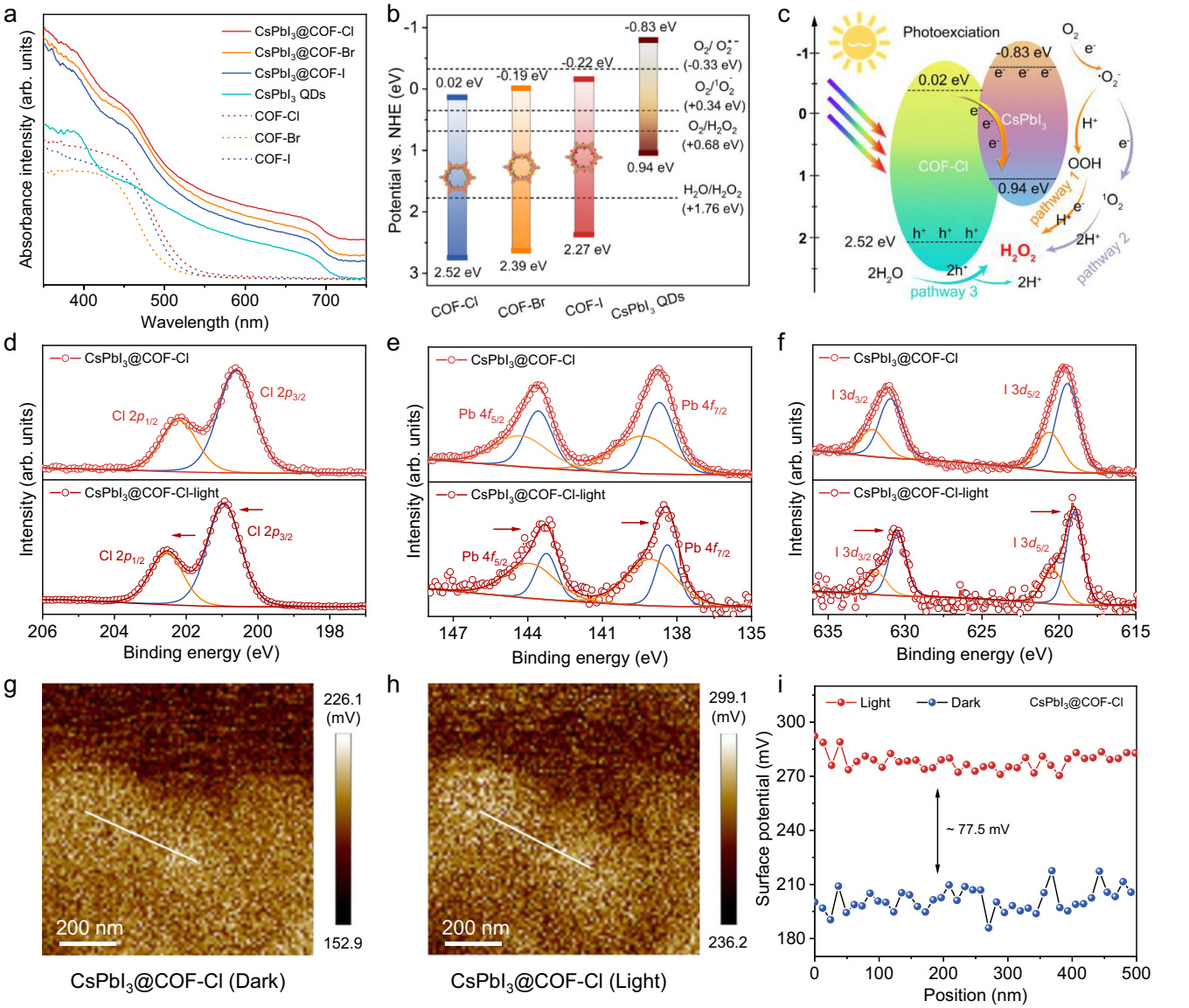

Fig. 4 | Characterizations of the optical properties for $CsPbI_3$ QDs, COF-X matrix and $CsPbI_3$@COF-X system. a UV-vis DRS spectra of $CsPbI_3$ QDs, COF-X matrix and $CsPbI_3$@COF-X system. **b** Electronic band structures for $CsPbI_3$ QDs and COF-X matrix (versus NHE). **c** Schematics of photocatalytic H_2O_2 production over $CsPbI_3$@COF-Cl system. **d** XPS Cl 2*p* spectra $CsPbI_3$@COF-Cl system. **e** XPS Pb 4*f* spectra $CsPbI_3$@COF-X system. **f** XPS I 3*d* spectra of $CsPbI_3$@COF-Cl system. **g** Surface potential maps of $CsPbI_3$@COF-Cl system in dark. **h** Surface potential maps of $CsPbI_3$@COF-Cl system under light irradiation. **i** Potential difference distribution of the $CsPbI_3$@COF-Cl system in the dark and light. Source data are provided as a Source Data file.

charge transfer in $CsPbI_3$@COF-Cl compared to COF-Cl alone. Pure $CsPbI_3$ QDs were excluded due to their aqueous instability. Electrochemical impedance spectroscopy (EIS) further confirms reduced charge-transfer resistance in $CsPbI_3$@COF-Cl, evidenced by a smaller Nyquist semicircle (Fig. S45).

The interfacial electron transfer mechanism in the $CsPbI_3$@COF-Cl heterojunction was demonstrated by Ultraviolet photoelectron spectroscopy (UPS). The results are displayed in Figs. S46, S47. The work functions of $CsPbI_3$ QDs and COF-Cl are 5.83 eV and 7.00 eV, respectively. Correspondingly, the Fermi levels of $CsPbI_3$ QDs and COF-Cl are −5.83 eV and −7.00 eV (vs vacuum level), respectively. This work function disparity establishes a higher Fermi level in $CsPbI_3$ QDs than in COF-Cl, driving electron migration from $CsPbI_3$ QDs to COF-Cl upon heterojunction formation[21]. This initial electron transfer leads to charge redistribution at the interface, establishing a unified Fermi level, an internal electric field (IEF)[22], and causing upward band bending in $CsPbI_3$ QDs and downward band bending in COF-Cl. Further validation through in-situ XPS under light illumination tracked binding energy shifts in key elements. As shown in Fig. 4d, light exposure caused the Cl 2*p* peaks in $CsPbI_3$@COF-Cl to shift from 202.2 eV and 200.6 eV to 202.6 eV and 201.0 eV, indicating electron loss from the COF-Cl component. Simultaneously, the Pb 4*f* peaks shifted from 144.29 eV/139.42 eV and 143.57 eV/138.70 eV to 143.92 eV/139.05 eV and 143.25 eV/138.38 eV (Fig. 4e), while the I 3*d* peaks shifted from 632.12 eV/620.62 eV and 630.95 eV/619.45 eV to 632.46 eV/619.96 eV and 630.46 eV/618.96 eV (Fig. 4f). These shifts collectively confirm electron gain by the $CsPbI_3$ QDs component. Therefore, photogenerated electrons transfer from COF-Cl to $CsPbI_3$ QDs under light excitation, directly evidencing the S-scheme charge transfer process. The combined UPS and in-situ XPS results provide direct experimental evidence for the charge transfer process and quantitatively support the proposed S-scheme mechanism initiated by the Fermi level offset (Fig. S48). Initially, the Fermi level difference drives the flow of electrons from $CsPbI_3$ QDs to COF-Cl, thereby forming the IEF. This leads to an upward band bending in $CsPbI_3$ QDs and a downward band bending in COF-Cl at the interface. Under illumination, the IEF, Coulomb

attraction, and band bending promote recombination of COF-Cl conduction band electrons with $CsPbI_3$ valence band holes.

To further explore carrier transfer mechanisms, femtosecond transient absorption (fs-TA) spectroscopy was employed to analyze the dynamics of photogenerated charge carriers using a 400 nm pump pulse. The fs-TA spectra of $CsPbI_3$ QDs (Fig. S49a, b) exhibit characteristic ground-state bleaching (GSB) at 460 − 600 nm and photoinduced absorption (PIA) at 600 − 700 nm, with decay kinetics (Fig. S49c) fitting to $\tau_1 = 13.19$ ps and $\tau_2 = 243.50$ ps. For COF-Cl (Fig. S50a, b), two distinct GSB signals are observed at 460 − 560 nm and 630 − 700 nm, with kinetics (Fig. S50c) described by $\tau_1 = 5.95$ ps and $\tau_2 = 184.90$ ps. In the $CsPbI_3$@COF-Cl system (Fig. S51a, b), key spectral changes confirm the S-scheme mechanism: the electron-related signal of COF-Cl (630 − 700 nm) is completely quenched, and the hole-associated PIA signal of $CsPbI_3$ QDs (600 − 700 nm) is strongly suppressed. This simultaneous quenching provides direct evidence that electrons from COF-Cl recombine with holes from $CsPbI_3$ QDs at the interface. The kinetic analysis (Fig. S51c) further supports this model, revealing a shortened decay component ($\tau_2 = 67.55$ ps) indicative of accelerated interfacial recombination, and the emergence of a long-lived component ($\tau_3 = 934.40$ ps) corresponding to the stabilized useful charges—electrons in $CsPbI_3$ QDs and holes in COF-Cl.

Moreover, in-situ irradiated Kelvin Probe Force Microscopy (KPFM) was employed to monitor the surface photovoltage (SPV) changes of the heterojunction material (Fig. 4g, h). Upon light irradiation, the surface potential of $CsPbI_3$@COF-Cl exhibited a notable increase from 198.6 mV to 276.1 mV, corresponding to an SPV change of 77.5 mV (Fig. 4i). This increase indicates effective suppression of charge carrier recombination. In contrast, pristine COF-Cl alone showed negligible SPV change (Fig. S52). More specifically, the accumulation of photo-generated holes in the valence band of the surface-exposed COF-Cl component provides evidence for an S-scheme heterojunction mechanism, wherein electrons from COF-Cl recombine with holes from the $CsPbI_3$ QDs. This interpretation is further supported by control experiments on a deliberately synthesized $CsPbI_3$-COF-Cl composite, in which perovskite was grown on the outer surface of COF-Cl (Fig. S53). In this configuration, a clear SPV increase on COF-Cl accompanied by a reduced SPV response from the $CsPbI_3$ was observed, reinforcing those holes accumulate in COF-Cl while electrons are retained within the $CsPbI_3$ QDs under illumination. This mechanism retains useful electrons in the CB of $CsPbI_3$ QDs and holes in the VB of COF-Cl, maximizing their redox potential for enhanced photocatalytic oxygen reduction.

Full reaction photosynthesis of H_2O_2 on a three-phase interface

The $CsPbI_3$@COF-Cl system demonstrates significant potential for the photocatalytic synthesis of H_2O_2, as its energy band structure is sufficiently capable of driving both essential half-reactions: the oxidation of H_2O ($E(H_2O_2/H_2O) = +1.76$ V vs. NHE, pH = 0) and the reduction of O_2 ($E(H_2O_2/O_2) = +0.68$ V vs. NHE, pH = 0)[23]. This indicates its theoretical suitability as an effective photocatalyst for the full photosynthetic reaction producing H_2O_2. Cyclic voltammetry (CV) further elucidates these redox capabilities. As shown in Fig. S54, the CV curve identifies a reduction potential of −0.94 V (vs. Ag/AgCl, pH = 7), corresponding to −0.33 V vs RHE (pH = 0), assigned to the reduction of O_2 to $\bullet O_2^-$. Simultaneously, an oxidation potential of +1.15 V (vs. Ag/AgCl, pH = 7), equivalent to +1.76 V vs RHE (pH = 0), is observed for the oxidation of H_2O to H_2O_2. Therefore, the combined theoretical and electrochemical data confirm that the $CsPbI_3$@COF-Cl system can effectively drive the photochemical synthesis of H_2O_2 using only water and atmospheric oxygen.

Photocatalytic H_2O_2 generation was evaluated in both pure water and seawater under visible-light irradiation and ambient air, without sacrificial agents, employing the iodometric method for quantitative determination (Fig. S55). Benefiting from its lightweight nature and hydrophobicity, the $CsPbI_3$@COF-Cl system readily spreads across the water surface, facilitating redox reactions at this air-solid-liquid interface (Fig. S22). The reduction of charge transfer resistance by over 70% under the floating configuration provides direct evidence that the formation of an efficient gas-solid-liquid triphase interface enhances the reaction kinetics (Fig. S23). Under air in pure water, the H_2O_2 yield showed clear accumulation over time, exhibiting a near-linear relationship between production and irradiation duration for both the COF-Cl matrix alone and the $CsPbI_3$@COF-Cl system (Fig. 5a). This indicates sustained high photosynthetic rates even under prolonged illumination. After 1 h, H_2O_2 yields reached 15.57 mmol g^{-1} h^{-1} for COF-Cl and 25.29 mmol g^{-1} h^{-1} for $CsPbI_3$@COF-Cl system, respectively (Fig. S56). This significant enhancement in the $CsPbI_3$@COF-Cl system is attributed to optimized charge separation efficiency achieved through interfacial band engineering, coupled with efficient O_2 diffusion in the three-phase (gas-solid-liquid) reaction system. Conversely, when evaluated in a diphase (liquid-solid) system, the H_2O_2 production rate showed a decrease of more than 68% (Fig. S57), underscoring that limited O_2 supply becomes a critical bottleneck when the advantageous three-phase interface is absent. Given this promising performance, we systematically evaluated H_2O_2 production under seawater and air conditions (Fig. 5b). After 1 h of photochemical conversion, H_2O_2 yields of 12.52 mmol g^{-1} h^{-1} and 20.37 mmol g^{-1} h^{-1} were achieved for the COF-Cl matrix and the $CsPbI_3$@COF-Cl system, respectively (Fig. S58). During the photocatalytic process, Cl_2 was not monitored by online mass spectrometry (MS) (Fig. S59). The progressive accumulation of oxidative chlorine species, as quantified by the DPD (*N, N*-diethyl-p-phenylenediamine) method (Fig. S60) and shown by the increase from 5.2 ppm to 6.4 ppm over the reaction period (Fig. S61), confirms chloride oxidation as a competing side reaction.

The apparent quantum yield (AQY) action spectrum of the $CsPbI_3$@COF-Cl system was measured across the visible range (Fig. 5c, and tabulated in Table S9) under ambient atmospheric conditions, yielding values of 15.45% at 420 nm and 15.76% at 450 nm. The trend of photocatalytic efficiency closely follows the composite's own absorption profile (Fig. 5c), rather than that of the individual $CsPbI_3$ QDs or COF-Cl components. This correlation provides direct evidence that the high activity originates from the integrated light-harvesting and charge generation of the formed S-scheme heterojunction as a whole. We note that obtaining a reliable AQY for pristine $CsPbI_3$ QDs in aqueous media was not feasible due to their rapid degradation, which itself underscores the critical stabilizing role of the COF-Cl matrix.

Cycling stability tests confirmed the system's durability. The $CsPbI_3$@COF-Cl system maintained stable H_2O_2 production performance over five consecutive photocatalytic cycles in seawater under air (Figs. S62, S63). TEM imaging and XRD analysis revealed no significant structural changes or deposition of insoluble salts (e.g., Mg/Ca hydroxides/carbonates) after cycling in seawater (Figs. S64, S65), highlighting its robustness against fouling. Post-cycling XPS analysis confirms the chemical stability of $CsPbI_3$@COF-Cl, as the characteristic dual-doublet peaks of Pb, I, and Cl remain intact after five catalytic runs (Fig. S66), supporting its stable cycling performance. To further verify operational stability in seawater, a continuous 20 h photocatalytic reaction was conducted (Fig. 5d), demonstrating stable H_2O_2 production. PXRD measurements during operation further confirmed structural stability under prolonged seawater exposure (Fig. 5e). To assess the environmental safety and practical viability, the reaction solution from the 20 h stability test was analyzed by inductively coupled plasma mass spectrometry (ICP-MS). The leaching concentrations of Pb^{2+} and Cs^+ were quantified as 0.64 ppm and 1.52 ppm, respectively. The Pb^{2+} concentration falls below the 1.0 ppm limit of China's Integrated Wastewater Discharge Standard (GB 8978-1996), which is attributed to the effective stabilization via Cl-Pb coordination and the hydrophobic barrier of the COF-Cl matrix. Neat $CsPbI_3$ QDs rapidly degrade in water

https://doi.org/10.1038/s41467-026-70503-2

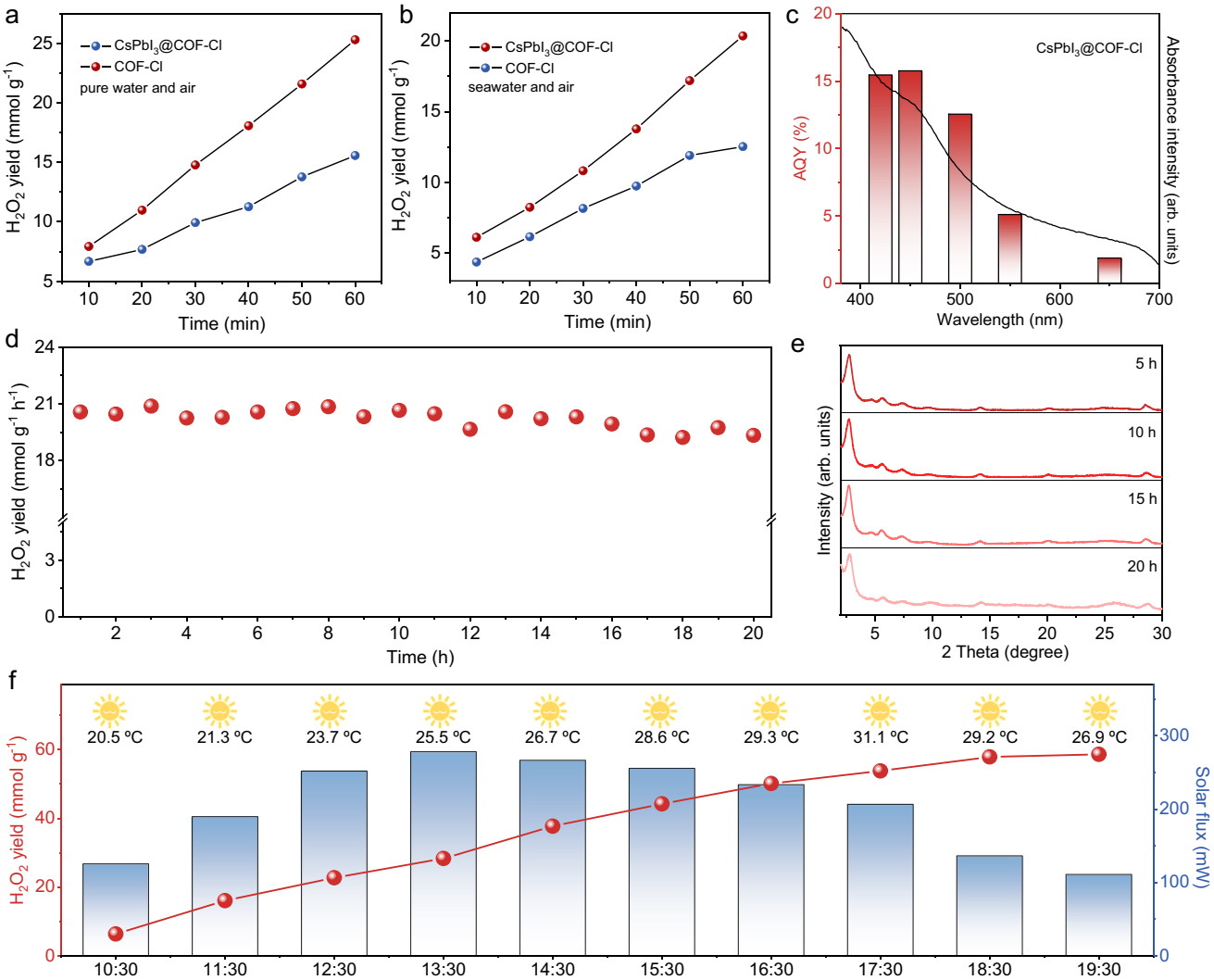

Fig. 5 | Photocatalytic H_2O_2 production over COF-Cl matrix and $CsPbI_3$@COF-Cl system. a Kinetic curves of H_2O_2 generation in pure water under air. **b** Kinetic curves of H_2O_2 generation in seawater under air. **c** Wavelength-dependent AQY values and UV-vis DRS of the $CsPbI_3$@COF-Cl system. **d** Long-term stability test: Continuous H_2O_2 production over $CsPbI_3$@COF-Cl system under visible-light irradiation for 20 h. **e** PXRD patterns of the $CsPbI_3$@COF-Cl system over time, confirming structural stability. **f** Outdoor experiment: H_2O_2 yield, system temperature, and light intensity recorded over time for $CsPbI_3$@COF-Cl system. The production rate in (**a**, **b**, **d**–**f**) and AQY data in (**c**) are from a single measurement. Source data are provided as a Source Data file.

(Fig. S67), while the control composite $CsPbI_3$-COF-H, without halogen modification, with perovskite poorly encapsulated and predominantly in the inactive δ-phase on the surface (Fig. S68), exhibits negligible performance (Fig. S69).

To demonstrate practical solar-to-chemical energy conversion, the H_2O_2 production performance of $CsPbI_3$@COF-Cl was evaluated under natural sunlight in Lanzhou City, P. R. China (May 1, 2025; Figs. 5f, S70). Real-time monitoring was carried out to track solar irradiance at 450 nm, system temperature, and H_2O_2 yield. After 10 h, an accumulated H_2O_2 concentration of 11.7 mmol L^{-1} was achieved, confirming efficient photocatalytic activity under real-world conditions. Combined with its high efficiency, these findings indicate that the $CsPbI_3$@COF-Cl system holds significant promise for large-scale, solar-driven H_2O_2 production from pure water and natural seawater. This performance is competitive among reported photocatalysts (Fig. S71, Table S10)[24–45]. The $CsPbI_3$@COF-Cl system achieved solar-to-chemical conversion (SCC) efficiency of 1.38%, while competitive among direct photosynthesis systems, is primarily limited by the suboptimal utilization of the full solar spectrum, optical losses at the triphase interface, and the kinetic overpotentials required to drive the dual $2e^-$ ORR and WOR pathways simultaneously.

To elucidate the reaction mechanism of hydrogen peroxide (H_2O_2) generation, electron paramagnetic resonance (EPR) spectroscopy was employed to detect key intermediates during photochemical conversion. Using 2,2,6,6-tetramethylpiperidine-N-oxyl (TEMP) as a spin trap for singlet oxygen ($^1O_2$) and 5,5-dimethyl-1-pyrroline N-oxide (DMPO) for superoxide anion radicals ($\bullet O_2^-$), distinct signals for DMPO-$\bullet O_2^-$ and TEMP-$^1O_2$ adducts were observed (Fig. 6a, b)[46]. The $CsPbI_3$@COF-Cl system exhibited stronger intermediate signals than COF-Cl alone. Superoxide ($\bullet O_2^-$), a key intermediate in H_2O_2 generation via oxygen reduction reactions (ORR), forms through $O_2 + e^- \rightarrow \bullet O_2^-$ (electrode potential: −0.33 V vs. RHE, pH = 0) and subsequently reacts via $\bullet O_2^- + e^- + 2H^+ \rightarrow H_2O_2$. Singlet oxygen ($^1O_2$) is generated by $\bullet O_2^-$ oxidation by photogenerated holes (h^+): $\bullet O_2^- + h^+ \rightarrow {}^1O_2$, a pathway consistent with prior reports on photocatalytic H_2O_2 production[47]. Furthermore, $^1O_2$ contributes to H_2O_2 formation through a two-electron reduction: ${}^1O_2 + 2e^- + 2H^+ \rightarrow H_2O_2$. Alternatively, H_2O_2 can form directly via a two-electron ORR: $O_2 + 2e^- + 2H^+ \rightarrow H_2O_2$ (0.68 V vs. RHE, pH = 0). The significant EPR signals for both $^1O_2$ and $\bullet O_2^-$ observed in the $CsPbI_3$@COF-Cl system demonstrate that H_2O_2 generation proceeds via both pathways, contributing to its enhanced photosynthetic efficiency. We also explored

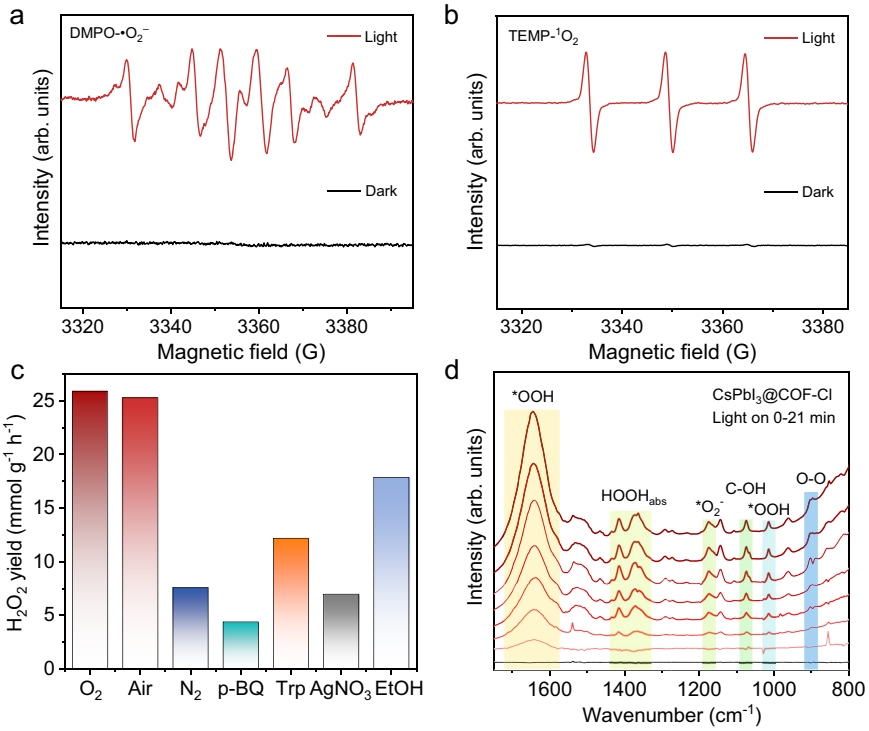

Fig. 6 | Mechanistic investigations of the photocatalytic H_2O_2 production over the $CsPbI_3$@COF-Cl system. a EPR spectra using DMPO as a spin-trapping agent for $•O_2^-$ under dark conditions and visible light illumination. **b** EPR spectra using TEMP as a spin-trapping agent for $^1O_2$ under dark conditions and visible light illumination. **c** H_2O_2 yields in the presence of O_2, Air, N_2 and specific scavengers: p-benzoquinone (p-BQ, $•O_2^-$ scavenger), L-tryptophan (Trp, $^1O_2$ scavenger), silver nitrate ($AgNO_3$, electron (e^-) scavenger), and ethanol (EtOH, hole (h^+) scavenger). **d** Time-course in situ DRIFTS of the $CsPbI_3$@COF-Cl system under visible-light irradiation in an O_2 atmosphere. The production rate in (**c**) is from a single measurement. Source data are provided as a Source Data file.

the contribution of the water oxidation reaction (WOR) to H_2O_2 production. Previous studies indicate that water can react with holes to form hydroxyl radicals ($H_2O + h^+ \rightarrow •OH + H^+$), which dimerize to produce H_2O_2 ($2•OH \rightarrow H_2O_2$)[22]. This process has a standard electrode potential of 2.72 V vs. RHE (pH = 0). However, no •OH signals are detected in the $CsPbI_3$@COF-Cl system, as their VB positions are more negative than the standard redox potential of H_2O/•OH, rendering them thermodynamically incapable of oxidizing H_2O to generate •OH radicals[21]. Alternatively, H_2O_2 can be generated directly from water and holes ($2H_2O + 2\,h^+ \rightarrow H_2O_2 + 2H^+$; E = 1.76 V vs. RHE, pH = 0), suggesting WOR also contributes to H_2O_2 formation. Isotopic labeling using $H_2{}^{18}O$ under anaerobic conditions confirmed the direct formation of $H_2{}^{18}O_2$ (Fig. S72), providing definitive evidence that H_2O_2 originates from water oxidation, while MS analysis simultaneously verified the absence of competing O_2 or H_2 evolution (Fig. S73).

To validate this hypothesis and explore alternative H_2O_2-production pathways, a series of control experiments was performed over the $CsPbI_3$@COF-Cl system. As shown in Fig. 6c, p-benzoquinone (p-BQ), L-tryptophan (Trp), $AgNO_3$, and ethanol (EtOH) were employed as scavengers for $•O_2^-$, $^1O_2$, e^-, and h^+, respectively[48]. The addition of p-BQ drastically reduced the H_2O_2 yield, underscoring the critical role of $•O_2^-$ in H_2O_2 generation. Similarly, Trp moderately suppressed H_2O_2 production, confirming the participation of $^1O_2$ in the formation process. Furthermore, while $AgNO_3$ and EtOH also diminished H_2O_2 yields, a significant amount of H_2O_2 persisted, suggesting that both e^- and h^+ contribute to but are not solely responsible for H_2O_2 production. Moreover, controlled anaerobic/aerobic experiments quantitatively show that the water oxidation pathway contributes ~29.3% to the total H_2O_2 yield (Fig. 6c), confirming its role as a significant secondary channel.

Supporting evidence for surface intermediates was obtained through in-situ diffuse reflectance infrared Fourier transform spectroscopy (DRIFTS) under visible-light irradiation in the presence of H_2O and O_2 (Fig. 6d). The appearance of a C–OH vibration peak (1077 cm^{-1}) confirms the presence of adsorbed *OH species, likely formed by H_2O dissociation[49]. Furthermore, characteristic vibration signals of *OOH (1647 and 1013 cm^{-1}) were detected, demonstrating the activation of adsorbed O_2 by photogenerated electrons (e^-) to form *OOH intermediates[50]. Moreover, the signals of O-O stretching mode (890–921 cm^{-1}) gradually increased[51–53].

To gain theoretical insight into possible reaction pathways, density functional theory (DFT) calculations were performed to estimate the Gibbs free energy (ΔG) for the adsorption of intermediates (*O_2, *OOH, *OH) at distinct sites on the $CsPbI_3$@COF-Cl system during both the oxygen reduction reaction (ORR) and water oxidation reaction (WOR) pathways for photocatalytic H_2O_2 synthesis (Fig. S74). These pathways involve intermediates and reaction steps. For the ORR process, O_2 undergoes conversion to *O_2 and *OOH, followed by *OOH protonation to yield H_2O_2. As visualized in Fig. S74a, the model predicts that both *O_2 and *OOH adsorb preferentially on $CsPbI_3$ QDs. The computed energy barriers for these steps are −0.44 eV and −0.88 eV, respectively, suggesting a possible synergistic role of the S-scheme heterojunction in reducing the overall reaction energy barrier in silico. Conversely, the WOR pathway involves H_2O dehydrogenation to *OH (the rate-determining step) followed by *OH dimerization to form H_2O_2. Fig. S74b illustrates that, according to the calculation, *OH adsorbs exclusively on COF-Cl sites, with an estimated energy barrier of 1.72 eV for the initial dehydrogenation step. These theoretical results are consistent with the interpretation that the $CsPbI_3$@COF-Cl system may favor adsorptions of *OOH (ORR) and *OH (WOR) intermediates. Under visible light, photogenerated electrons and holes separate via the S-scheme heterojunction and migrate to $CsPbI_3$ QDs and COF-Cl, respectively, enabling simultaneous ORR and WOR. If the computed pathway is operative, on $CsPbI_3$ QDs, ORR proceeds

through $*O_2$ hydrogenation to *OOH and subsequent protonation to H_2O_2. Meanwhile, WOR on COF-Cl involves H_2O dehydrogenation to *OH ($\Delta G = 1.72$ eV), followed by *OH coupling. Critically, protons released during WOR are consumed in ORR, maintaining charge balance. Taken together, the computational models suggest that the S-scheme heterojunction in $CsPbI_3$@COF-Cl could accelerate charge separation, potentially facilitating O_2 reduction by electrons and H_2O oxidation by holes to generate reactive intermediates, thereby contributing to efficient H_2O_2 production.

Discussion

This work establishes a multifunctional interfacial engineering strategy that stabilizes $CsPbI_3$ quantum dots within a hydrophobic chlorine-functionalized covalent organic framework (COF-Cl), enabling efficient and durable photosynthesis of H_2O_2 from seawater. Our strategy leverages multisite atomic-chlorine passivation, simultaneously forming Cl–I halogen bonds and Cl–Pb coordination bonds, to suppress ionic migration and defect-induced recombination. Concurrently, the COF-Cl matrix creates a gas-solid-liquid triphase interface that enhances O_2 diffusion while isolating $CsPbI_3$ from aqueous degradation. Additionally, the system forms an S-scheme heterojunction that spatially separates charge carriers: electrons accumulate on $CsPbI_3$ for selective $2e^-$ oxygen reduction ($O_2 \rightarrow H_2O_2$), while holes localize on COF-Cl to drive water oxidation ($H_2O \rightarrow H_2O_2$), all without sacrificial agents. The system achieves H_2O_2 production rates of 20.37 mmol h^{-1} g^{-1} in natural seawater, with an apparent quantum yield of 15.76% at 450 nm and a solar-to-chemical conversion efficiency of 1.38%. Structural integrity is maintained over multiple cycles, and outdoor testing confirms operational viability under natural sunlight. Mechanistic studies confirm synergistic proton-coupled electron transfer, where holes on COF-Cl oxidize H_2O to supply protons for O_2 reduction on $CsPbI_3$ QDs, balancing reaction kinetics. This work presents a design for perovskite-based artificial photosynthesis in corrosive environments, demonstrating competitive efficiency and stability in solar-driven chemical production. The multifunctional passivation strategy, integrating atomic-scale defect control, tailored interfaces, and directional charge separation, may support the development of scalable solar fuel synthesis from abundant seawater resources.

Methods

Materials and chemicals

2,5-Dichloroterephthalaldehyde (PDA-Cl, 95%), 2,5-dibromoterephthalaldehyde (PDA-Br, 95%), and 2,5-diiodoterephthalaldehyde (PDA-I, 95%) were obtained from Zhongke Yanshen Technology Co., Ltd. (Jilin, China). Lead(II) iodide (PbI_2, 99.99%) was procured as perovskite-grade reagents from Tokyo Chemical Industry (TCI). Cesium iodide (CsI, 99.99%) and L-tryptophan (Trp, 99%) was obtained from Aladdin Industrial Corporation. Nafion (5 wt%), oleic acid (OA, 90%) and oleylamine (OAm, 98%) were purchased from Sigma-Aldrich. Terephthalaldehyde (TPA, 98%), 4-Aminobenzonitrile ($C_7H_6N_2$, 98%), trifluoromethanesulfonic acid (CF_3SO_3H, 98%), 2,2,6,6-tetramethylpiperidine (TEMP, 99%), 5,5-dimethyl-1-pyrroline N-oxide (DMPO, 97%), Heavy-oxygen water ($H_2{}^{18}O$, 97 atom % ^{18}O), N, N-diethyl-p-phenylenediamine sulfate ($C_{10}H_{18}N_2O_4S$, 98%), o-dichlorobenzene (o-DCB, 98%) and p-benzoquinone (p-BQ, 99%) were acquired from Macklin Biochemical Co., Ltd. Potassium iodide (KI, analytical grade) was supplied by Cologne Chemicals Co., Ltd. Potassium hydrogen phthalate ($KHC_8H_4O_4$, 99.9%) was purchased from Tianjin Chemical Reagent Research Institute. The anhydrous potassium dihydrogen phosphate (KH_2PO_4, 99.5%), disodium ethylenediaminetetraacetate (Na_2EDTA, 99%), anhydrous disodium hydrogen phosphate (Na_2HPO_4, 99%), silver nitrate ($AgNO_3$, 99.8%) and hydrogen peroxide (H_2O_2, 30%) were purchased from Chron Chemicals (Chengdu, China). N,N-dimethylformamide (DMF, 99.8%, Extra Dry. with molecular sieves) was purchased from Energy Chemical. N-butanol (n-BuOH, 99.5%), acetic acid (AcOH, 99.5%), ethanol (EtOH, 99.7%), toluene (Tol, 99.5%), anhydrous methanol (MeOH, 99.5%) and tetrahydrofuran (THF, 99.5%) was supplied by Rionlon BoHua (Tianjin) Pharmaceutical & Chemical Co., Ltd. All electrolytes were prepared fresh prior to each experiment and used immediately. All chemicals were used as received without any further purification.

Characterization

The sample morphology was examined using a field emission scanning electron microscope (FE-SEM; FEI Sirion 200). Transmission electron microscopy (TEM) and high-resolution TEM (HRTEM) analyses were conducted on an FEI Tecnai G2-F30 electron microscope at an accelerating voltage of 300 kV and on an FEI Talos 200s electron microscope operating at an accelerating voltage of 200 kV. Powder X-ray diffraction (PXRD) patterns were obtained using an AXS D8-Advanced diffractometer with Cu-Kα radiation. Nitrogen adsorption-desorption measurements were performed on a fully automated surface area and porosity analyzer (ASAP 2020 M); the specific surface area was calculated based on the Brunauer-Emmett-Teller (BET) model, and the pore size distribution was evaluated using the non-local density functional theory (NLDFT) model. X-ray photoelectron spectroscopy (XPS), valence band XPS (VB XPS), and ultraviolet photoelectron spectroscopy (UPS) measurements were carried out using a PHI5702 multifunctional spectrometer with Al-Kα radiation. The light source used for the in situ XPS measurements was a 300 W xenon lamp (HSX-UV300, Beijing NBeT Technology Co., Ltd.), identical to the illumination source employed in our photocatalytic H_2O_2 synthesis experiments. Fourier-transform infrared (FTIR) spectra at room temperature were recorded on a Nicolet FT-170SX spectrometer. In-situ diffuse reflectance infrared Fourier transform spectroscopy (DRIFTS) was performed on a FTIR spectrometer (Bruker, INVENIO R) equipped with an MCT detector and cooled using LN2. Thermogravimetric (TG) analysis was performed using a TGA/DSC3 + /Sartorius/MCA125S-2CCN-1 thermogravimetric/differential thermal analyzer. Contact angle measurements were conducted using an SZ-CAMB3 instrument. Ultraviolet-visible (UV-vis) spectroscopy was carried out using a spectrophotometer (Thermo Fisher Scientific Genesys 10S UV-vis) with a 1 cm path length cuvette. Photoluminescence (PL) spectra were acquired on an Edinburgh Instruments FLS920 fluorescence spectrometer. Time-resolved fluorescence decay spectra (TRFDS) were collected using an Edinburgh Instruments FLS920 steady-state fluorescence spectrometer and a transient fluorescence spectrometer, respectively. Solid-state UV-Vis diffuse reflectance spectra (UV-vis DRS) were measured using a UV-2006 ultraviolet spectrophotometer. The light source used in our experiments was a 300 W xenon lamp (HSX-UV300) from Beijing NBeT Technology Co., Ltd. Electron paramagnetic resonance (EPR) spectroscopic measurements were performed at room temperature using a CIQTEK EPR100 spectrometer. The ultrafast transient absorption (fs-TA) measurements were conducted using a laser system consisting of a Coherent Legend Elite regenerative amplifier (1 kHz, 800 nm), seeded by a Coherent Chameleon oscillator (120 fs, 80 MHz). The pump pulses included the fundamental 800 nm output from the amplifier and its 400 nm harmonic generated via a BBO crystal. Additional pump wavelengths across 290–2600 nm were provided by a Light Conversion Oper A-Solo optical parametric amplifier. A broadband probe beam spanning from UV to NIR (350–1600 nm) was employed. The Kelvin probe force microscopy (KPFM) tests were conducted on the Bruker Dimension Icon, using a 300 W xenon light source with a wavelength of 420 nm. Inductively coupled plasma optical emission spectrometry (ICP-OES) was employed to quantitatively determine the concentrations of metal ions. Products were monitored in real time using mass spectrometry (MS) (Omnistar, PFEIFFER). The photoelectrochemical properties of the samples were tested using a CHI760E electrochemical workstation (Shanghai Chenhua Instrument Co., Ltd, China). Photocatalytic tests were performed

using a xenon lamp (HSXF/UV 300) equipped with 400–800 nm filters. Proton nuclear magnetic resonance (^{1}H NMR and ^{13}C NMR) spectra were acquired on a JEOL ESC 400 M instrument using tetramethylsilane (TMS) as the internal standard. Time-resolved spectra were fitted with a triexponential function, and the average lifetime was calculated using the following formula. Standard silica particles dispersed in water were used as the reference.

$$A(t) = A_1 \exp\left(-\frac{t}{t_1}\right) + A_2 \exp\left(-\frac{t}{t_2}\right) + A_3 \exp\left(-\frac{t}{t_3}\right) \quad (1)$$

$$\tau_{av} = \frac{A_1\tau_1^2 + A_2\tau_2^2 + A_3\tau_3^2}{A_1\tau_1 + A_2\tau_2 + A_3\tau_3} \quad (2)$$

$$A_1' = \frac{A_1\tau_1}{A_1\tau_1 + A_2\tau_2 + A_3\tau_3} \quad (3)$$

$$A_2' = \frac{A_2\tau_2}{A_1\tau_1 + A_2\tau_2 + A_3\tau_3} \quad (4)$$

$$A_3' = \frac{A_3\tau_3}{A_1\tau_1 + A_2\tau_2 + A_3\tau_3} \quad (5)$$

Synthesis of 2,4,6-tris(4-aminophenyl)−1,3,5-triazine (TAPT)

A solution was prepared by adding 2.0 g (17.0 mmol) of 4-aminobenzonitrile to a 50 mL round-bottom flask and cooling it in an ice bath at 0 °C for 30 min. Under a nitrogen atmosphere, 5.0 mL (55.5 mmol) of trifluoromethanesulfonic acid was slowly added dropwise, maintaining the temperature at 0 °C throughout the addition. Upon completion, the reaction mixture was poured into 50 mL of deionized water. The mixture was then neutralized to pH 7 using a 2 mol·L^{-1} NaOH solution, resulting in the formation of a pale yellow precipitate. This precipitate was collected by filtration and purified through multiple washes with distilled water to afford the TAPT product.

Synthesis of COF-H framework

The COF-H frameworks were synthesized by dissolving TAPT (0.16 mmol, 56.7 mg) and TPA (0.24 mmol, 32.2 mg) in a pressure-resistant glass tube containing a 1:1 (v/v) mixture of o-dichlorobenzene and n-butanol (1.0 mL each). The mixture was sonicated for 5 min to enhance dissolution. Subsequently, 0.2 mL of 6 mol·L^{-1} acetic acid solution was added quickly, followed by brief sonication 10 s. The glass tube was then subjected to three freeze-pump-thaw cycles under liquid nitrogen and vacuum, sealed, and heated in an oil bath at 120 °C for 72 h. After cooling to room temperature (~25 °C), the resulting yellow product was collected by centrifugation, thoroughly washed with tetrahydrofuran and methanol, and purified by Soxhlet extraction to yield the COF-H framework.

Synthesis of COF-X (X = Cl, Br, I) frameworks

The COF-X frameworks were synthesized by dissolving TAPT (0.16 mmol, 56.7 mg) and the appropriate dialdehyde monomer (0.24 mmol) in a pressure-resistant glass tube containing a 1:1 (v/v) mixture of o-dichlorobenzene and n-butanol (1.0 mL each). The dialdehyde monomers used were: 2,5-dichloroterephthalaldehyde (PDA-Cl, 48.7 mg) for COF-Cl, 2,5-dibromoterephthalaldehyde (PDA-Br, 70.1 mg) for COF-Br, and 2,5-diiodoterephthalaldehyde (PDA-I, 92.6 mg) for COF-I. The mixture was sonicated for 5 min to enhance dissolution. Subsequently, 0.2 mL of 6 mol·L^{-1} acetic acid solution was added quickly, followed by brief sonication (10 s). The glass tube was then subjected to three freeze-pump-thaw cycles under liquid nitrogen and vacuum, sealed, and heated in an oil bath at 120 °C for 72 h. After cooling to room temperature (~25 °C), the resulting yellow product was collected by centrifugation, thoroughly washed with tetrahydrofuran and methanol, and purified by Soxhlet extraction to yield the COF-X framework (The atomic coordinates of COF-X are listed in Tables S11–13).

Preparation of $CsPbI_3$@COF-X artificial photosynthetic systems

For each $CsPbI_3$@COF-X system, 50 mg of COF-X (X = Cl, Br, I) powder was immersed in 2.5 mL of a 0.04 mol·L^{-1} PbI_2 solution in N,N-dimethylformamide (DMF). The suspension was sonicated for uniform dispersion and reacted at 70 °C for 2 h. The resulting solid, designated as PbI_2@COF-X, was collected and washed repeatedly with DMF and ethanol to remove surface-adsorbed PbI_2. This intermediate was then immersed in 2.5 mL of a 0.02 mol·L^{-1} CsI solution in DMF for 1 h. Following this, 10 µL of oleic acid (OA) and 5 µL of oleylamine (OM) were added to stabilize the precursor mixture. Toluene was then added to induce the formation of $CsPbI_3$ quantum dots (QDs) within the pores of the COF-X framework. The final $CsPbI_3$@COF-X material was collected by centrifugation, washed thoroughly with toluene three times, and dried.

Photochemical H_2O_2 production test under simulated sunlight

The photocatalytic performance for H_2O_2 production was evaluated using a 5 mg sample of the $CsPbI_3$@COF-X artificial photosynthetic system dispersed in a double-layered reaction beaker containing 20 mL of either deionized water or seawater (0.25 g·L^{-1}). The reaction mixture was gently shaken to ensure uniform dispersion of the photocatalyst on the water surface. A thermostatic circulating water system maintained the reaction temperature at 25 °C. Photoreactions were conducted in air using a quartz and Pyrex glass hybrid reaction cell (Fig. S75). Irradiation was provided by a 300 W xenon lamp. Throughout the reaction, the temperature was maintained at 25 °C using a stirrer and the circulating water system. At 10-min intervals, a 1.5 mL aliquot of the reaction solution was extracted, centrifuged, and filtered through a 0.22 µm membrane to remove the photocatalyst. The hydrogen peroxide concentration in the filtrate was quantified using the iodometric method.

Catalyst recovery procedure for cyclic stability tests

The highly hydrophobic $CsPbI_3$@COF-Cl composite spontaneously forms a continuous film at the air-water interface during photocatalytic operation. For catalyst recovery in the cyclic stability tests, a sequential separation protocol was employed to ensure near-quantitative retrieval. First, the majority of the floating catalyst was gently collected from the water surface using a fine-mesh stainless steel scoop. Subsequently, the remaining reaction mixture was passed through a polyvinylidene fluoride (PVDF) microporous membrane (pore size: 0.22 µm) under mild vacuum to capture any residual catalyst particles. The recovered catalyst was then rinsed lightly with deionized water and dried at 60 °C under vacuum for 2 h before being used in the next catalytic cycle. This combined approach achieves efficient catalyst recovery without the need for high-speed centrifugation, underscoring a practical advantage of the interfacial reaction system.

H_2O_2 detection

The hydrogen peroxide (H_2O_2) content was determined using the iodometric method[54]. Briefly, 1 mL of potassium iodide solution (0.4 mol·L^{-1}) and 1 mL of potassium hydrogen phthalate solution (0.1 mol·L^{-1}) were mixed, followed by the addition of 0.5 mL of the centrifuged reaction supernatant. The mixture was allowed to stand for 30 min to ensure the complete reaction of H_2O_2 with I^- under acidic conditions, generating I_3^- ($H_2O_2 + 3I^- + 2H^+ \rightarrow I_3^- + 2H_2O$). The absorbance of I_3^- was then measured at 350 nm using UV-visible

spectroscopy, and the H_2O_2 concentration was quantified based on a standard curve.

Total chlorine detection

The total chlorine content was determined using the N,N-diethyl-p-phenylenediamine (DPD) spectrophotometric method. Specifically, 2.00 mL of the sample was mixed with 0.1 mL of phosphate buffer (pH ~5.8) and 0.1 mL of DPD indicator solution. Then, 0.2 mL of potassium iodide solution (100 g·L^{-1}) was added. The mixture was allowed to stand for 2 min to ensure complete oxidation of iodide by chlorine species to iodine, which subsequently reacted with DPD to form a red-colored complex. The absorbance of the complex was measured at 515 nm using a UV-Vis spectrophotometer. The total chlorine concentration was quantified based on a standard curve prepared with chlorine standards.

Apparent quantum yield (AQY) measurement

The AQY of H_2O_2 over $CsPbI_3$@COF-Cl was measured under irradiation through different wavelength bandpass filters (420, 450, 500, 550 and 650 nm). All measurements were conducted in ambient air at standard atmospheric pressure. The photon flux of incident light was measured by an NBT 300 UV photo radiometer. The AQY was calculated according to the following Eq. (6)[55]:

$$\mathrm{AQY}(\%) = \frac{N_h}{N_p} \times 100\% = \frac{2 \times N_A \times M \times h \times c}{P \times S \times \lambda \times t} \times 100\% \quad (6)$$

Where N_h is the amount of reaction holes, N_p is the number of incident photons, N_A is the Avogadro constant (6.022×10^{23}/mol), M is the molar amount of H_2O_2 (mol), h is the Planck constant (6.626×10^{-34} J s), c is the speed of light (3×10^8 m/s), P is the intensity of the irradiation (W m^{-2}), S is the irradiation area (m^2), λ is the irradiation wavelength (m), and t is the irradiation time (s). The amounts of H_2O_2 produced and the light intensity of monochromatic light illumination are tabulated in Table S9.

Solar-to-chemical conversion

The solar-to-chemical conversion (SCC) efficiency was determined using a 300 W xenon lamp was used as the light source and calculated according to the following equation[55]

$$\mathrm{SCC\ efficiency}(\%) = \frac{\left[\Delta G for\ H_2O_2\ generation\ \left(J\ mol^{-1}\right)\right] \times [H_2O_2\ formed\ (mol)]}{[Total\ input\ power\ (W)][Reaction\ times\ (s)]} \times 100\% \quad (7)$$

The free energy for H_2O_2 formation is 117 kJ mol^{-1}.

Photoelectrochemical and electrochemical characterization

Photoelectrochemical and electrochemical properties were characterized using a standard three-electrode system with an Ag/AgCl reference electrode, a platinum sheet counter electrode, and an FTO conductive glass working electrode coated with the catalyst. The working electrode was prepared by dispersing 5 mg of the photocatalytic material in 0.5 mL of an ethanol/isopropanol mixture (3:1 v/v), sonicating for 30 min, adding 20 µL of Nafion solution, and sonicating for an additional 30 min. A 50 µL aliquot of the resulting catalyst slurry was uniformly coated onto the FTO glass and dried at 60 °C for 2 h. A 300 W xenon lamp with a 400 nm cutoff filter served as the light source. Transient Photocurrent Response: Measured in 0.1 mol·L^{-1} Na_2SO_4 electrolyte under light illumination. Mott-Schottky (MS) Analysis: Conducted in 0.1 mol·L^{-1} Na_2SO_4 electrolyte at frequencies of 500 Hz, 1000 Hz, and 1500 Hz, scanning the potential from −1.6 V to +1.6 V vs. Ag/AgCl. Electrochemical Impedance Spectroscopy (EIS): Performed in 0.1 mol·L^{-1} Na_2SO_4 electrolyte over a frequency range of 10^5 to 10^{-2} Hz.

Data availability

All data supporting the findings of this study are available within the article and its Supplementary Information. Any additional relevant data are available from the corresponding authors. Source data are provided with this paper.

References

1. Zhang, C. et al. Stable and high-yield hydrogen peroxide electrosynthesis from seawater. *Nat. Sustain.* **8**, 542–552 (2025).
2. Xia, C. et al. Direct electrosynthesis of pure aqueous H_2O_2 solutions up to 20% by weight using a solid electrolyte. *Science* **366**, 226–231 (2019).
3. Campos-Martín, J. M., Blanco-Brieva, G. & Fierro, J. L. G. Hydrogen peroxide synthesis: an outlook beyond the anthraquinone process. *Angew. Chem. Int. Ed.* **45**, 6962–6984 (2006).
4. Wang, W. et al. Photothermal-enabled single-atom catalysts for high-efficiency hydrogen peroxide photosynthesis from natural seawater. *Nat. Commun.* **14**, 2493 (2023).
5. Huang, W. et al. Intermarrying MOF glass and lead halide perovskites for artificial photosynthesis. *J. Am. Chem. Soc.* **174**, 3195–3205 (2024).
6. Zhao, W. et al. Perovskite-doped modulated color-selective photosynaptic transistors for target object recognition. *Nano lett* **24**, 9937–9945 (2024).
7. Sun, K. et al. Three-dimensional direct lithography of stable perovskite nanocrystals in glass. *Science* **375**, 307–310 (2022).
8. Hou, J. et al. Liquid-phase sintering of lead halide perovskites and metal-organic framework glasses. *Science* **374**, 621–625 (2021).
9. Tian, T. et al. Large-area waterproof and durable perovskite luminescent textiles. *Nat. Commun.* **14**, 234 (2023).
10. Fan, X. et al. Brightened bicomponent perovskite nanocomposite based on forster resonance energy transfer for micro-LED displays. *Adv. Mater.* **35**, e2300834 (2023).
11. Jiang, W. et al. Axial alignment of covalent organic framework membranes for giant osmotic energy harvesting. *Nat. Sustain.* **8**, 446–455 (2025).
12. Suleman, S. et al. Turning on singlet oxygen generation by outer-sphere microenvironment modulation in porphyrinic covalent organic frameworks for photocatalytic oxidation. *Angew. Chem. Int. Ed.* **63**, e202314988 (2024).
13. Li, P. et al. Development of an energy-dense and high-power Li-Cl_2 battery using reversible interhalogen bonds. *Chem* **10**, 352–364 (2023).
14. Wu, J. et al. Regioselective multisite atomic-chlorine passivation enables efficient and stable perovskite solar cells. *J. Am. Chem. Soc.* **145**, 5872–5879 (2023).
15. Liu, Y. et al. Halogen atom-induced local asymmetric electron in covalent organic frameworks boosts photosynthesis of hydrogen peroxide from water and air. *Matter* **8**, 102076 (2025).
16. Zhang, L. et al. Deep-red emissive colloidal lead-based triiodide perovskite/telluride nanoscale heterostructures with reduced surface defects and enhanced stability for indoor lighting applications. *Nano Energy* **90**, 106506 (2021).
17. Wang, A. et al. Halogenated hole selective contact enhances interfacial weak bonding of perovskite solar cells. *Adv. Energy Mater.* **14**, 2400640 (2024).
18. He, J. et al. Competitive formation mechanism for bidentate passivation of halogen vacancies in perovskite based on 6-chloropurine. *Small* **20**, 2305127 (2023).
19. Fu, X. et al. Halogen-halogen bonds enable improved long-term operational stability of mixed-halide perovskite photovoltaics. *Chem* **7**, 3131–3143 (2021).

20. Wang, P. et al. Ultrastable perovskite-zeolite composite enabled by encapsulation and in situ passivation. *Angew. Chem. Int. Ed.* **59**, 23100–23106 (2020).
21. Qiu, J. et al. COF/In_2S_3 S-scheme photocatalyst with enhanced light absorption and H H_2O_2-production activity and fs-TA investigation. *Adv. Mater.* **36**, e2400288 (2024).
22. Li, F. et al. Understanding the unique S-scheme charge migration in triazine/heptazine crystalline carbon nitride homojunction. *Nat. Commun.* **14**, 3901 (2023).
23. Zhang, Y. et al. H_2O_2 generation from O_2 and H_2O on a near-infrared absorbing porphyrin supramolecular photocatalyst. *Nat. Energy* **8**, 361–371 (2023).
24. Cao, D. et al. Hydroxyl-functionalized donor-acceptor covalent organic frameworks for efficient photocatalytic hydrogen peroxide production under visible light. *ACS Catal* **15**, 3584–3594 (2025).
25. Yu, Z. et al. Amidoxime-functionalized sp^2-carbon-conjugated covalent organic frameworks for overall photocatalytic hydrogen peroxide production. *Adv. Sci.* **12**, e2415194 (2025).
26. Shi, X. et al. Interfacial engineering of β-ketoenamine-based COFs/urea-linked perylene diimide for overall photosynthesis of H_2O_2 in seawater. *Adv. Funct. Mater.* **35**, 2414755 (2024).
27. Yue, J. Y. et al. One-pot synthesis of fully conjugated covalent organic frameworks via the pictet–spengler reaction for boosting H_2O_2 photogeneration in real seawater. *Adv. Funct. Mater.* **35**, 2421514 (2025).
28. Hou, Y. et al. Building a confluence charge transfer pathway in COFs for highly efficient photosynthesis of hydrogen peroxide from water and air. *Angew. Chem. Int. Ed.* **64**, e202505621 (2025).
29. Yue, J. Y. et al. Thiophene-containing covalent organic frameworks for overall photocatalytic H_2O_2 synthesis in water and seawater. *Angew. Chem. Int. Ed.* **62**, e202309624 (2023).
30. Huang, Y. et al. Nb_2C MXene quantum dots modulate the built-in electric field within heterostructures for efficient solar-to-H_2O_2 conversion from seawater. *Appl. Catal. B Environ.* **371**, 125262 (2025).
31. Yue, J.-Y. et al. Overall solar H_2O_2 generation in water and real seawater by covalent organic frameworks with kgd topology. *Chem. Eng. J.* **504**, 158983 (2025).
32. Tang, B. et al. Photocatalytic synthesis of hydrogen peroxide by rhenium modified metal-organic frameworks incorporating bianthracene ligands. *J. Am. Chem. Soc.* **174**, 24326–24335 (2025).
33. Hu, Z. Y. et al. Binder-free immobilization of photocatalyst on membrane surface for efficient photocatalytic H_2O_2 production and water decontamination. *Nanomicro Lett.* **17**, 301 (2025).
34. Ju, Y. et al. Regulating the electronic structure of covalent organic frameworks via heterocyclic isomers for highly efficient photocatalytic H_2O_2 generation. *Nat. Commun.* **16**, 5658 (2025).
35. Zhou, J. et al. Covalent organic frameworks with constrained palladium nanoclusters lock the enol-keto tautomerism, enhancing hydrogen peroxide photosynthesis. *Small* **21**, e2409006 (2025).
36. Sun, M. et al. Bifunctional Pd-O_x center at the liquid-solid-gas triphase interface for H_2O_2 photosynthesis. *ACS Catal* **12**, 2138–2149 (2022).
37. Yan, S. et al. Photocatalytic H_2O_2 generation reaction with a benchmark rate at air-liquid-solid joint interfaces. *Adv. Mater.* **36**, e2307967 (2024).
38. Ma, D. et al. Precise regulation of Zn, S dual vacancies in $Zn_3In_2S_6$ inducing local orientated electrical field for photocatalytic H_2O_2 generation. *Angew. Chem. Int. Ed* **65**, e21029 (2025).
39. Tang, Y. Y. et al. Molecular engineering of metal-organic frameworks for boosting photocatalytic hydrogen peroxide production. *Angew. Chem. Int. Ed.* **63**, e202408186 (2024).
40. Sun, R. et al. Carbazole-containing covalent triazine frameworks for efficient hydrogen peroxide photosynthesis from natural sunlight. *Chem. Eng. J.* **490**, 151332 (2024).
41. Yu, B. et al. Breathing air into water: dual-pathway H_2O_2 synthesis via aerating amphiphilic supramolecular films. *Energ. Environ. Sci.* **18**, 8382–8390 (2025).
42. He, M. et al. Gas/solid/liquid triphase interface of carbon nitride for efficient photocatalytic H_2O_2 production. *Inorg. Chem. Front.* **12**, 3237–3245 (2025).
43. Liu, Z. et al. Efficient hydrogen peroxide generation utilizing photocatalytic oxygen reduction at a triphase interface. *iScience* **17**, 67–73 (2019).
44. Zhang, C. et al. Synthesis of InP quantum dot decorated Bi_2WO_6 microspheres for the efficient photocatalytic production of hydrogen peroxide in water. *J. Alloy. Compd.* **1011**, 178253 (2025).
45. Chen, Z. et al. Nitrogen heterocyclic covalent organic frameworks for efficient H_2O_2 photosynthesis and in situ water treatment. *Nat. Commun.* **16**, 6943 (2025).
46. Chen, J. et al. Redox-mediated TEMPO-based donor-acceptor covalent organic framework for efficient photo-induced hydrogen peroxide generation. *Angew. Chem. Int. Ed.* **64**, e202500924 (2025).
47. Gu, M. et al. Efficient sacrificial-agent-free solar H_2O_2 production over all-inorganic S-scheme composites. *Appl. Catal. B Environ.* **324**, 122227 (2023).
48. Luo, Y. et al. Sulfone-modified covalent organic frameworks enabling efficient photocatalytic hydrogen peroxide generation via one-step two-electron O_2 reduction. *Angew. Chem. Int. Ed.* **62**, e202305355 (2023).
49. Zhou, S. et al. Chloromethylation modified pyranonitrile-based conjugated microporous polymers for selective one-step two-electron O_2 reduction to H_2O_2. *Angew. Chem. Int. Ed.* **64**, e202508436 (2025).
50. Wang, W. et al. Graphene quantum dot-modified $Mn_{0.2}Cd_{0.8}S$ for efficient overall photosynthesis of H_2O_2. *Adv. Funct. Mater.* **35**, 2422307 (2025).
51. Xu, T. et al. Constructing photocatalytic covalent organic frameworks with aliphatic linkers. *J. Am. Chem. Soc.* **146**, 20107–20115 (2024).
52. Li, Z. et al. Covalent organic frameworks for boosting H_2O_2 photosynthesis via the synergy of multiple charge transfer channels and polarized field. *Angew. Chem. Int. Ed.* **64**, e202420218 (2025).
53. Liu, R. et al. Linkage-engineered donor-acceptor covalent organic frameworks for optimal photosynthesis of hydrogen peroxide from water and air. *Nat. Catal.* **7**, 195–206 (2024).
54. Li, Y. et al. Constructing a solid-gas-interfacial Fenton reaction over alkalinized-C_3N_4 photocatalyst to achieve an apparent quantum yield of 49% at 420 nm. *J. Am. Chem. Soc.* **138**, 13289–13297 (2016).
55. Liu, J. et al. Constructing donor-acceptor covalent organic frameworks for highly efficient H_2O_2 photosynthesis coupled with oxidative organic transformations. *Angew. Chem. Int. Ed* **64**, e202416240 (2025).

Acknowledgments

The work was financially supported by the National Natural Science Foundation of China (grant no. 22377047 [B.D. Wang], 22221001 [B.D. Wang], and 223B2204 [H. Wang]), Science and Technology Leading Talent Foundation of Gansu Province (grant no. 24RCKB003 [B.D. Wang]). We gratefully acknowledge the insightful guidance on heterojunction structures provided by Prof. Y. Ding. We also thank Dr. S.Y. Wang for the assistance with ultrafast transient absorption (fs-TA) measurements and Dr. X. Fang for the help with in situ irradiated Kelvin Probe Force Microscopy (KPFM) tests. We are also grateful to the Electron Microscopy Center and the Analysis and Testing Center of Lanzhou University for their assistance.

Author contributions

B.D. Wang led the project, supervised the experimental work, and revised the manuscript. B.D. Wang and G.P. Meng designed the project and wrote the paper. G.P. Meng carried out the materials synthesis, characterization, experimental test, and data analysis. S. Wei performed experiments, interpreted the results, and revised the paper. N. Li conducted theoretical calculations and established models with G.P. Meng. H. Wang conducted the in situ DRIFTS experiment and revised the paper. G.P. Meng, S. Wei, Y.H. Yin, B. Dong, S.H. Sun and G.W. Hu performed the electron microscopy tests. All the authors contributed to the discussion during the whole project.

Competing interests

The authors declare no competing interests.

Additional information

Supplementary information The online version contains supplementary material available at https://doi.org/10.1038/s41467-026-70503-2.

Correspondence and requests for materials should be addressed to Hao Wang or Baodui Wang.

Peer review information *Nature Communications* thanks Qianrong Fang and the other anonymous reviewer(s) for their contribution to the peer review of this work. A peer review file is available.